Journal of Materials Chemistry B

# Synergistic Effect of Inductive and Conductive Factors in Gelatin-Based Cryogels for Bone Tissue Engineering



| | |
|---|---|
| Journal: | *Journal of Materials Chemistry B* |
| Manuscript ID | TB-ART-11-2015-002496.R2 |
| Article Type: | Paper |
| Date Submitted by the Author: | 26-Jan-2016 |




| | |
|---|---|
| Complete List of Authors: | Liao, Han- Tsung ; Chang Gung University, Department of Chemical and Materials Engineering; Chang Gung Memorial Hospital<br>Shalumon, K.T. ; Chang Gung University, Department of Chemical and Materials Engineering<br>Chang, Kun- Hung ; Chang Gung University, Department of Chemical and Materials Engineering<br>Sheu, Chialin ; Chang Gung University, Department of Chemical and Materials Engineering<br>Chen , Jyh-Ping ; Chang Gung University, Department of Chemical and Materials Engineering; Chang Gung University of Science and Technology |

# Synergistic Effect of Inductive and Conductive Factors in Gelatin-Based Cryogels for Bone Tissue Engineering

*Han- Tsung Liao[a,b,#], K.T. Shalumon[a,#], Kun- Hung Chang[a], Chialin Sheu[a], Jyh-Ping Chen[a,c]**

[a]*Department of Chemical and Materials Engineering, Chang Gung University, Kwei-San, Taoyuan 333, Taiwan, Republic of China*

[b]*Department of Plastic and Reconstructive Surgery, Chang Gung Memorial Hospital, Chang Gung University, College of Medicine, Kwei–San, Taoyuan 333, Taiwan, Republic of China*

[c]*Graduate Institute of Health Industry and Technology, Research Center for Industry of Human Ecology, Chang Gung University of Science and Technology, Kwei-San, Taoyuan 333, Taiwan, Republic of China*

[#] Han-Tsung Liao and K.T. Shalumon contributed equally to this work

[*]Corresponding author: Tel: +886–3–2118800; fax: +886–3–2118668; e–mail: jpchen@mail.cgu.edu.tw

## Abstract

Macroporous and biocompatible scaffolds for bone tissue engineering were prepared from 4% gelatin (G) and 4% gelatin/2% nanohydroxyapatite (nHAP) (GN), by cryogelation. The cryogels are with interconnected pores with pore size around 100 μm and a high degree of cross-linking. Incorporation of nHAP slightly reduced the porosity, degree of crosslinking, swelling kinetics and equilibrium water uptake, but enhanced the toughness of the cryogel scaffolds. The osteo-regeneration potential of GN cryogel was further enhanced by binding with bone morphogenetic protein (BMP-2) to produce the gelatin/nHAP/BMP-2 (GNB) scaffold. Efficacy of BMP-2 incorporation was tested through in vitro release studies and a sustained release profile could be observed from the cumulative BMP-2 release curve. To elucidate the effect of cryogel composition on cell proliferation and differentiation, rabbit adipose-derived stem cells (ADSCs) were seeded in cryogel scaffolds. In vitro studies demonstrated reduced proliferation rate and enhanced osteogenic differentiation of ADSCs in GNB cryogel scaffolds from the combined effect of nHAP and BMP-2, judging from the elevated alkaline phosphatase activity and degree of mineralization. Confocal microscopy confirmed high viability and good cytoskeletal spreading of ADSCs on cryogels while osteocalcin (OCN) protein quantification affirmed the dominance of GNB in osteogenic differentiation of ADSCs compared to G and GN cryogels. The maximum osteogenesis capability of GNB was also confirmed through up-regulation of specific bone maker genes of early marker protein collagen I (COL I) and late marker protein osteopontin (OPN). From in vivo animal model, the computed tomography analysis confirmed the superior bone regeneration capability of ADSCs in GNB cryogels by implanting ADSCs/GNB cryogel constructs in rabbit critical size calvarial defects. Histological and immuno-histochemical analysis demonstrated new bone formation and continued expression of COL I and OCN bone-specific proteins at the defect site. Taken together, the results demonstrate that G cryogels modified with osteo-conductive nHAP and osteo-inductive BMP-2 could provide cues to synergistically promote osteogenesis of ADSCs in vitro and in vivo.


**Keywords:** Gelatin; nanohydroxyapatite; bone morphogenic protein; cryogel; bone tissue engineering

## 1. Introduction

Tissue engineering is an emerging area in the twenty-first century to meet the increasing demands of tissue repair or organ replacement. It combines engineering and biology through advances in cell, molecular biology and biomaterials.[1] It could surpass the limitations of conventional treatments like organ transplantation and biomaterial implantation through repair of tissues like skin,[2] liver,[3] bone,[4] cartilage[5] etc. Like other tissue engineering approaches, bone tissue engineering also uses healthy cells from the host tissue, which are seeded in scaffolds made from natural or synthetic polymers. The cell/scaffold construct cultured in vitro will be implanted in the defective site in vivo to repair or regenerate bone tissue.

The major challenges in developing a suitable bone scaffold is its bio-compatibility, biodegradability, pore size, pore connectivity and adequate mechanical strength.[6] Polymers used for this purpose are usually biodegradable materials such as poly(glycolic acid) (PGA),[7] poly(lactic acid) (PLA)[8] and their copolymers poly(lactic acid-glycolic acid) (PLGA),[9] poly(caprolactone) (PCL)[10] etc., as degradation products of all these materials could be easily removed from the body, without affecting the physiological functions. However, most of the polymers have relatively poor mechanical strength or bio-inert behavior,[11] which could slow down the regeneration process than required. Furthermore, a polymer alone cannot provide the ideal scaffold for bone tissue engineering since it is neither osteo-conductive nor osteo-inductive in nature.

Various natural polymers have been reported to fabricate bone tissue engineering scaffolds.[12] Gelatin is considered as one of the ideal natural polymers to be used in bone tissue engineering scaffold preparation due to its biodegradability, biocompatibility, cost efficiency, processability and resemblance in structure to the major organic component of the bone matrix (i.e. collagen).[13-15] Gelatin is reported to be efficient in the fabrication of other tissue engineering scaffolds too.[5, 16]. Various processing methods such as freeze drying,[17] gas foaming,[18] particulate leaching,[19] phase separation[20] etc. have been adopted in the preparation of porous scaffolds. Most of the methods are simple and economical towards the fabrication of porous scaffolds. However, compared to other techniques, cryogelation that could produce macroporous cryogel scaffolds is more reliable and reproducible to fabricate an ideal three-dimensional (3D) porous structure.

Natural bone consists of organic and inorganic components, in which calcium phosphate in the form of nanohydroxyapatite (nHAP) takes the major share of the inorganic part.[21] When

considering the fabrication of tissue engineered bone constructs, nHAP can be chosen as an osteo-conductive material to be incorporated in the scaffold.[22] Thus, nHAP is widely regarded as an ideal candidate to be incorporated in bone-scaffold due to its superior bioactivity, biocompatibility, osteo-conductivity, osteo-integration and non-toxicity. A polymer-ceramic composite scaffold would resemble the natural bone structure with nHAP embedded in the collagen matrix. The size, morphology of the particles and pores in the scaffold can influence the biological response of the scaffold material.[23] The optimum pore size for tissue regeneration depends on the cell type; however, an interconnected pore structure with a pore size in the range of 100-500 μm is considered optimal for nutrient transfer and osteo-conduction for optimal tissue growth.[24]

Apart from nHAP, bone regeneration is also regulated by various growth factors like bone morphogenetic proteins (BMPs)[25], transforming growth factor,[26] fibroblast growth factor,[27] platelet-derived growth factor[28] and insulin-like growth factor.[29] These growth factors can create an osteogenic microenvironment to enhance bone reconstruction and scaffolds containing them could easily perform protein therapy. Among all the growth factors, BMPs could promote differentiation by inducing stem cells to transform into osteoblasts, and then to bone. In this study, we report the fabrication of gelatin-based tissue engineering cryogel scaffolds for bone reconstruction and also discuss the added benefit of incorporation of nHAP in the gelatin scaffold for bone regeneration. We already demonstrated the advantages of gelatin-based cryogels in various tissue reconstruction applications, in our previous results.[30, 31] Enhanced bone regeneration was further planned by introducing BMP-2. The function of nHAP in the gelatin scaffold is to keep a proper balance between the biological and the mechanical properties, while BMP-2 triggers the osteogenic differentiation. Influence of BMP-2 and nHAP on cell proliferation and differentiation of ADSCs were evaluated both in vitro and in vivo by focusing on osteogenesis in a rabbit calvarial (skull) defect model. In short, the purpose of this study is to evaluate the synergistic effect of both inductive and conductive factors in a single scaffold material, towards bone regeneration.

## 2. Materials and methods

### 2.1. Materials

Dulbecco's modified Eagle's medium (DMEM) was purchased from Sigma, while fetal bovine serum (FBS) was obtained from HyClone. 2-morpholinoethane sulfonic acid (MES), gelatin (type A from porcine skin, 300 bloom) and 2,4,6-trinitrobenzene sulfonic acid (TNBS) were purchased from Sigma. 1-Ethyl-3-(3-dimethylaminopropyl) carbodiimide (EDC) and N-hydroxysuccnimide (NHS) were obtained from Acros. 4',6-Diamidino-2-phenylindole dihydrochloride (DAPI) and rhodamine-phalloidin were purchased from Life Technologies. Recombinant human bone morphogenetic protein-2 (BMP-2) was obtained from Sino Biological Inc. (China).

### 2.2. Preparation of gelatin (G) and gelatin/nHAP (GN) cryogels

Hydroxyapatite nanoparticles (nHAP) were synthesized as per standard protocols reported earlier.[32] The preparation of cryogels followed the same principle and similar procedures as reported in our previous works.[30,31] Cryogels containing 4% gelatin (G) and 4% gelatin/2% nHAP (GN) were prepared as per following procedures. Briefly, 8% gelatin or 8% gelatin/4% nHAP solution was prepared in 0.1 M MES buffer (pH 6.5) at 60 ºC. The solution was mixed gently with an equal volume of 2 mM EDC prepared separately in 0.l MES buffer (pH 6.5) at 37 ºC for 1 h. To complete the cross-linking process, the blend was immediately injected into the wells of a 48-well cell culture plate and placed in a -20 ºC deep freezer for another 16 h. The cryogel scaffolds were removed from the freezer, thawed at room temperature and washed thoroughly in de-ionized water to eliminate unreacted residues. After cutting with a sharp blade, disc-shaped cryogels (10 mm diameter × 5 mm thickness) were dried in a vacuum oven at 37ºC for 24 h and stored in a desiccator at room temperature.

### 2.3 Preparation of gelatin/nHAP/BMP-2 cryogel (GNB cryogel)

For covalent immobilization of BMP-2 to GN cryogel, 30 mg GN cryogel (10 mm diameter × 5 mm thickness) was activated in 1 ml of 0.1 M MES buffer (pH 6.0) containing 0.5 mg/ml EDC and 0.7 mg/ml NHS at 37 ºC for 30 min.[33] One microgram of BMP-2 was then added to the

solution and reacted for 2 h in an incubator shaken at 50 rpm and 37 ºC. The BMP-2 conjugated cryogel was thoroughly washed with deionized water to remove unbound BMP-2 and dried in vacuum. The amount of immobilized BMP-2 was determined from unreacted BMP-2 in the reacting and washing solutions with a BMP-2 ELISA kit from PeproTech (Rocky Hill, NJ, USA).

### 2.4. Characterization of cryogels

#### 2.4.1 Physico-chemical evaluation

The microstructure and elemental composition of cryogels was observed using a scanning electron microscope/energy dispersive spectrometer (SEM/EDS) (JEOL ISM-5410 SEM equipped with HORIBA EX-250 EDS). The porosity of the scaffolds was determined by the ethanol displacement method as described in our previous study.[30] Pore size measurement was carried out with capillary flow porometry (PMI CFP-1100-AI, Porous Materials Inc., USA) using ethanol as the wetting agent. The density of scaffold was calculated by the mass of the dry scaffold over its volume. The TNBS method was used to determine the degree of cross-linking (DC).[34] A standard curve generated using glucosamine was used to determine the presence of available free amino groups within a sample and the DC was calculated by DC (%) = [1-(free amino groups/mass)$_c$/(free amino groups/mass)$_{nc}$] × 100, where c and nc represent cross-linked and non-cross-linked samples, respectively. All physico-chemical property values reported are the mean ± SD of five independent measurements.

#### 2.4.2 FTIR analysis

Fourier transform infrared (FTIR) spectra were obtained using a Horiba 730 FTIR spectrometer. The cryogel sample was ground to a fine powder, mixed with KBr powder (1:8), dried in a 70 $^{o}$C oven for 24 h and compressed into pellets for FTIR examination over a wavenumber range between 400 and 4000 cm$^{-1}$ with a scanning speed of 2.5 cm$^{-1}$/s and a resolution of 2 cm$^{-1}$.

#### 2.4.3 XRD analysis

X-ray diffraction (XRD) analysis was done with a Siemens D5005 X-ray diffractometer (Germany) having a CuKa source, a quartz monochromater and a goniometric plate. The analysis was carried out with a scanning speed of 2º/min from 5 to 60º and the spectra were recorded as intensity vs 2θ value.

### 2.4.4 Swelling characteristics of cryogels

The conventional gravimetric procedure was used to determine the swelling of cryogels in water. The cryogel sample was dried at 60 ºC for 24 h before immersing in deionized water at room temperature. The weight of the swollen sample at different time intervals ($M_t$) and at 60 min after reaching equilibrium ($M_{eq}$) was determined. The water uptake (WU) could be calculated based on the dry weight of the samples ($M_d$) from equation (1).[35]

$$\mathrm{WU} = \frac{M_t - M_d}{Meq} \times 100 \qquad (1)$$

The water diffusion in the cryogel was determined by fitting the swelling kinetics with equation (2).[36]

$$\frac{M_t - M_d}{M_{eq} - M_d} \times 100 = kt^n \qquad (2)$$

where k, t and n are the rate constant, time and the exponent of the transport mode of water, respectively.

### 2.4.5 Thermogravimetric analysis

Thermal stability of the samples was analyzed through thermogravimetric analysis (TGA) (TGA 2050, TA Instruments, USA) under a nitrogen atmosphere. Samples were allowed to undergo a controlled heating at a rate of 10 °C/min from 25 °C to 600 °C. The weight loss or derivative weight loss was plotted against temperature to estimate the decomposition of cryogel at elevated temperatures.

### 2.4.6 Mechanical properties

The quasi-static and dynamic compression behavior of the cryogels was investigated using compression tests. The quasi-static unconfined compression test was conducted for wet cryogel (soaked in phosphate buffered saline (PBS) for 24 h before testing) samples at 37 °C using an ElectroForce®5200 BioDynamic™ testing machine (Bose). A 250 N load cell was used to provide a uniaxial stress to generate the stress–strain curves at a cross–head speed of 0.02 mm/sec. The strain was defined as $\varepsilon$ (mm/mm) = displacement (mm)/height (mm). The stress was defined as $\sigma$ (MPa)=force (N)/cross sectional area ($mm^2$). The ultimate stress and ultimate strain values were the point where failure of the cryogel sample occurred. The stress–strain data up to failure were curve–fitted according to the following non–linear equation,[37]

$$\sigma = Ae^{B\varepsilon - 1} \qquad (3)$$

where A and B are elastic constants. The tangential Young's (elastic) modulus (slope of the tangent to the stress–strain curve) at 30% and 50% strain was calculated using the non–linear elastic model. The toughness (compressive strain energy to failure) of a cryogel, which is the energy required to deform a sample to failure, was obtained from the area under the stress–strain curve. For the dynamic compression test, the wet cryogel sample was dynamically tested with sinusoidal compressions from 0.5 to 5 Hz at 30% strain and 5% dynamic amplitude strain. The dynamic mechanical analysis software measured the values of the storage modulus $E$ (the energy stored per cycle), $E''$ (the energy lost per cycle) and tan $\delta = E''/E'$ (viscous damping).

**2.4.7 BMP-2 release kinetics**

The release profile of BMP-2 was evaluated by immersing GNB cryogels in 1 ml PBS at 37 °C. The release medium was removed completely each day and replenished with fresh PBS. The concentration of BMP-2 in the release medium was determined by a BMP-2 ELISA kit from PeproTech (Rocky Hill, NJ, USA). Released BMP-2 (ng) at each time point was measured and the cumulative release percentage of BMP-2 with respect to time was calculated from the original amount of BMP-2 in the scaffold. The average values of six samples are reported.

**2.5 In vitro cell culture**

**2.5.1 Cell proliferation**

Isolation of rabbit adipose-derived stem cells (ADSCs) was carried out following the procedures reported previously.[38] ADSCs were seeded on pre-wetted cryogels (10 diameter × 5 mm thickness) at a seeding density of $5\times10^4$ cells/scaffold in a 24-well culture plate and incubated at 37 °C for 4 h to allow cell adhesion. The scaffold was transferred to a new well with the addition of 1.5 ml cell culture medium (DMEM, 10% FBS, 50 μM L-ascorbic acid phosphate, 0.1 μM dexamethasone, 10 mM glycerol 2-phosphate, and 1% antibiotic-antimycotic) into each well. Cell culture was carried out at 37 °C in a humidified 5% $CO_2$ incubator with medium change every 2 days. The proliferation rate of ADSCs on cryogel scaffolds was determined using the CellTiter 96® AQueous cell proliferation assay with a tetrazolium compound [3-(4,5-dimethylthiazol-2-yl)-5-(3-carboxymethoxyphenyl)-2-(4-sulfophenyl)-2H-tetrazolium, MTS]. The optical density (OD) of the solution was measured at 492 nm using an ELISA microplate reader (Synergy HT, BioTek, USA).

### 2.5.2 Alkaline Phosphatase (ALP) activity of ADSCs

The intracellular ALP activity of ADSCs was measured using an ALP kit (SensoLyte® pNPP ALP assay kit, AnaSpec, USA). At each time point, PBS washing was given to the samples (n=6) followed by immersion in a cell lysis solution containing 500 µl of 0.1% Triton X-100 and 5 mM $MgCl_2$. After centrifuged at 13,000 rpm for 10 min at 4ºC, 50 µl of the supernatant solution was mixed with 50 µl of p-nitrophenyl phosphate (5 mM) in 150 mM 2-amino-2-methyl-1-propanol buffer solution at room temperature for 30 min in dark. The reaction was stopped by adding 50 µl of 0.2 N NaOH and the OD was measured at 405 nm using an ELISA reader. The specific ALP activity per cell basis was reported by normalizing the ALP activity with the cell number from the MTS assay and expressed as $OD_{405}/OD_{492}$.

### 2.5.3 Mineralization of ADSCs with SEM/EDS

After PBS washing, cells were fixed using 4% glutaraldehyde and maintained in room temperature for 2 h. Following fixation, cryogels were washed with PBS three times and post-fixed with 1% $OsO_4$ (in 0.1 M phosphate buffer) at room temperature for 2 h. Another triplicate PBS washing was given to the membranes (20 min) prior to alcohol gradient dehydration (50, 70, 80, 90, 95, and 100% alcohol). Complete drying was achieved through a critical point dryer and the samples were sputter coated with gold at 30 mA for 60 s. Morphology of minerals deposited on the sample surface were monitored through SEM (Hitachi S-3000N SEM, Japan). Energy dispersive X-ray (EDX) analysis (HORIBA EX-250 EDS, Japan) for the atomic percentage of elements in mineral deposits was further used to confirm the mineral deposition on ADSCs.

### 2.5.4 Live/dead and cytoskeleton staining

Qualitative evaluation on the cell viability of ADSCs was assessed using the live/dead viability/cytotoxicity kit (Molecular probes, USA). After cultured for 21 days, the medium was removed and samples were washed three times with PBS. Live/dead staining solution was prepared with 2 µM calcein AM (excitation 494 nm, emission 517 nm) and 5 µM of ethidium homodimer-1 (EthD-1) (excitation 528 nm, emission 617 nm) in the culture medium, where the former is for detecting live cells and the latter is for dead cell identification. All the samples were incubated with the staining solution at 37 °C for 30 min in a 24-well plate and the morphology of cells was imaged under a Zeiss LSM 510 Meta confocal laser scanning microscope. The live and

dead cell morphologies were separately recorded and finally merged together to get a single image.

For the cytoskeletal staining, cell-seeded cryogel samples after 21 days were fixed in 0.5% paraformaldehyde in PBS for 30 min, followed by permeabilization in 0.1% Triton-X100 for 1 min. PBS washed scaffolds were then immersed in rhodamine-phalloidin solution (1:100 in PBS) for 30 min to stain actin cytoskeleton. Followed by PBS washing, the cell nucleus was further stained with 0.1 μg/ml DAPI in PBS for 5 min. The cells were visualized for its cytoskeletal arrangements using a confocal laser scanning microscope (Zeiss LSM 510 Meta) using the excitation and emission wavelengths of rhodamine-phalloidin at 540 and 340 nm and the same for DAPI at 573 and 488 nm, respectively.

**2.5.5 Osteocalcin quantification**

The osteogenic differentiation of ADSCs was examined by measuring the concentration of osteocalcin (OCN), a biochemical marker for bone formation, in the cryogel scaffold. The medium was removed after 7, 14 and 21 days of culture and the samples were washed twice with PBS. The amount of OCN was measured using a rabbit OCN ELISA kit from BlueGene Biotech., Shanghai, China.

**2.5.6 Osteogenic gene expression**

Expression of osteogenic differentiation marker genes was examined using standard protocols of RNA isolation and cDNA synthesis. RNA was isolated by immersing the cell-seeded samples in TRIzol (Invitrogen, USA). A mechanical membrane rupturing was given to the TRIzol immersed samples to ensure maximum cell retrieval and the corresponding solution was transferred to a 1.5 ml microcentrifuge tube. A high speed vortexing for 15~30 s was given to the tube after adding 200 μl chloroform to the cell suspension. The tube was placed in an ice bath for 5 min and centrifuged at 11,000 rpm for 15 min. RNA was isolated from the supernatant layer followed by reaction with isopropanol in 1:1 ratio at -80 °C for 30 minutes. The supernatant was removed and the solution was further centrifuged at 11000 rpm (4 °C) for 15 min. One ml of 75% ice cold ethanol was mixed at 4 ºC for 10 min, followed by centrifugation at 11000 rpm for 10 min. This step was repeated twice, followed by drying the final supernatant solution at room temperature. RNA was completely dissolved in 30 μl DEPC treated water (Invitrogen, USA) at 55 °C for 15 min. 1 μg of total RNA was reverse-transcripted into cDNA using SuperScript III RNase H

(Invitrogen, USA). Glyceraldehyde 3-phosphate dehydrogenase (GAPDH) was used as the housekeeping gene for internal control for analysis with a Bio-Rad software. Quantitative real time PCR (Q-PCR) measurements were performed using a SYBR Green RT-PCR kit (SYBR Green I supermix, Bio-Rad Laboratories Inc., Hercules, CA, USA) having a Mini Option detection system (Bio-Rad CFD-3120). Collagen type I (COL I) and osteopontin (OPN) bone marker genes were selected for analysis with the primer sequences reported before using the $2^{-\Delta\Delta ct}$ relative quantification method (n =6).[39]

**2.6 In vivo studies**

Animal studies were carried out as per the standards of the Association for Assessment and Accreditation of Laboratory Animal Care. The protocols were approved from the animal ethical committee of Chang Gung University. New Zealand white male rabbits weighing 3~4 kg were used for the study. All animals were kept in a single room and fed a dried diet and water ad libitum. The animals were injected with Atropin (0.3 mg/kg) intramuscularly first, followed by induction into general anesthesia with intramuscular injection of a mixture of Zoletil 50 (18 mg/kg) and Rompum 20 (1 mg/kg). After sterilization of scalp by betadine solution, a longitudinal incision was done over rabbit's scalp. Subperiosteal dissection was carried out, and the periosteum was reflected to expose the skull bony area. A 10-mm-diameter surgical trephine was then used to create 2 circular critical size defects and the bony discs were removed. The defects were chosen randomly, and one defect was filled with the acellular GNB cryogel (10 mm diameter × 5 mm thickness) and the other filled with ADSCs/GNB cryogel constructs. The ADSCs/cryogel construct was prepared by seeding $1\times 10^6$ ADSCs per cryogel scaffold (10 mm diameter × 5 mm thickness) and cultured in the cell culture medium for 21 days. The defects were filled so as to be in consistent contour with the surrounding bone. The surgical site was then closed with 4-0 Ethicon sutures.

All animals underwent postoperative computed tomography (CT) examination using a CT scanner (Somatom Sensation 16, Siemens) 1 week and 16 weeks post-operation. The CT image acquisition, processing, and manipulation were performed according to the standard protocol at a medical facility. The CT data were reformatted, and a voxel (unit of 3D image) was set at 0.6 mm × 0.6 mm × 0.6 mm for all scans. The imaging data were analyzed using the OsiriX Image software (Pixmeo, Bernex, Switzerland) for comparing the new bone regeneration

in 2D cross-sectional and 3D views in the calvarial defect. The cranial bone was extracted from the 3D CT images with the threshold adjusted to remove the soft tissue and display the bone density. The range of CT densities was fixed in all CT scans for cranial bone. Tissue mineral density was evaluated by Hounsfield unit (HU). Briefly, the OsiriX image software (Pixmeo, Bernex, Switzerland) was used to calculate the average HU value by outlining the region of interest (ROI) that was confined to the bone defect region in the 2D cross-sectional view. Each group was measured with eight repeats and normal bone surrounding the defect was measured as control. The new bone formation volume was calculated by the ROI manager built in the OsiriX Image software.

At 16 weeks post-operation, rabbits were euthanized with lethal doses of pentobarbital (0.5 g/kg body weight) and the implants were dissected out for gross evaluation. Samples were fixed in 10% formaldehyde, dehydrated, embedded in paraffin for sectioning. Five μm slice sections were subjected to hematoxylin and eosin (H&E), Masson's trichrome and immunohistochemical (IHC) staining of COL I and OCN.[32] The images were recorded under an inverted optical microscope (Olympus IX-71).

### 2.7 Statistical analysis

All quantitative data are reported as mean ± standard deviation. One-way ANOVA LSD test was used among multiple groups while Tukey's post hoc test was used to determine the difference between any two groups. A p value $< 0.05$ was considered statistically significant.

## 3. Results and discussions

### 3.1 Physico-chemical evaluation

The composition of G and GN cryogels were designed based on the optimal cryogel properties which could fulfill the minimal criteria of scaffolds intended for bone tissue engineering. The final mass ratio of gelatin to nHAP was determined to be 2:1 in which 50% ceramic counterparts compared to the organic polymer should intensify the osteo-conductivity of the scaffolds. Additionally, we expect the composite GN cryogel scaffolds incorporating the ceramic component nHAP could enhance the applicability G cryogel scaffolds for bone tissue repair with improved mechanical properties. Nonetheless, a dominance of nHAP in the composite might cause weakening of the scaffold due to brittle nature and low porosity. An optimum composition

of gelatin/nHAP ratio at 2:1 is expected to be coinciding with the mechanical as well as the slow degradation characteristics required for a bone tissue engineering scaffold through chemical cross-linking of gelatin with EDC.

The characteristics of nHAP were confirmed as reported in our previous study.[32] The prepared nHAP had a rounded morphology with the size of 49 ± 9 nm. The morphology of G and GN cryogel samples examined under SEM confirmed open interconnected pore morphology with both cryogels exhibited a pore size ranging from 100 to 150 μm **(Fig. 1a),** fulfilling the pore structure and pore size requirement for scaffolds intended for bone tissue engineering.[24] A minimum pore size between 100 and 150 μm was needed for bone formation and both cryogels apparently meet this criteria.[40] The calculated atomic percentages of Ca and P from the EDS **(Fig. 1a inserts**) are close to 0 for G cryogel. On the other hand, the Ca and P percentages for GN cryogel are 1.99% and 1.19%, respectively, matching the correct stoichiometric Ca/P ratio of nHAP at 1.67. Further experiments with capillary flow porosimetry provided the pore size distribution and the mean pore size. Both cryogels exhibit sharp pore size distribution with the minimum pore size being above 100 μm and G cryogel exhibited broader pore size distribution compared with GN cryogel **(Fig. 1b)**. However, the average pore sizes of G (112 ± 12 μm) and GN (108 ± 10 μm) cryogels were not significantly different, indicating the negligible influence of nHAP on cryogelation. This trend was also shown in porosity measurement where G cryogels had 91.0 ± 0.6% porosity while GN cryogels displayed a porosity of 87.9 ± 2.4%. An adequate porous structure is extremely important for cellular penetration into the scaffold and differentiation after cell seeding as high levels of porosity play a critical role in tissue formation.[41] The high porosity of both cryogels is therefore to be beneficial for its application as scaffold material intended for tissue repair. The trend of pore size distribution and porosity were reflected in the density measurements, in which G and GN cryogel showed densities of 120.6 ± 1.9 and 127.8 ± 1.4 mg/cm$^3$, respectively. The significantly higher density value of GN cryogel is attributed to the lower porosity and the presence of nHAP. The degree of crosslinking in G cryogel was 87.7 ± 0.3% while that in GN cryogel is 84.4 ± 0.2%. The significantly elevated crosslinking degree in G cryogel could be due to the efficient propagation of covalent linkages in the presence of EDC. On the other hand, the presence of nHAP could have hindered the effective

covalent crosslinking of gelatin macromolecules in GN cryogel thus led to reduced crosslinking efficiency.

### 3.2 FTIR and XRD analysis

FTIR was used to characterize the functional groups present in nHAP, G and GN cryogels. For nHAP, the characteristic stretching and bending vibrations at 877cm$^{-1}$ representing the carbonate ($CO_3^{2-}$) substitution whereas the phosphate ($PO_4^{3-}$) stretching vibrations were observed at 568, 609 and 1060 cm$^{-1}$ **(Fig. 2a)**. Additionally, the stretch bands at 1417 and 1471 cm$^{-1}$ confirm the presence of hydroxyl group and the broad bands observed at 1650 and 3440 cm$^{-1}$ indicate adsorbed water in nHAP. The peaks observed at 1517 and 1654 cm$^{-1}$ denote the amide I and amide II of G cryogel. For GN cryogel, all characteristic peaks corresponding to G cryogel and nHAP appear, indicating successful incorporation of nHAP into GN composite cryogel. The characteristic peak for nHAP at about 3570 cm$^{-1}$ (–OH stretching) was with decreased band intensity and broadening in GN, possibly due to the interaction between nHAP and gelatin.[42,43]

XRD analysis was also used to confirm the presence of nHAP in GN cryogels by observing the characteristic crystalline peaks **(Fig. 2b).** G cryogel gives a typical XRD pattern of partially crystalline structure of gelatin with a peak at 2θ = 21.5°, originated from the triple-helical crystalline structure in collagen and gelatin.[44] Thereafter, crosslinking with EDC apparently did not change the crystalline structure of gelatin in G cryogel. The XRD analysis of nHAP confirmed the formation of the apatite crystalline structure from the reflection peaks (JCPDS Card no. 9-432) at 2θ = 25.9°, 32.2°, 33.3°, 34.2, 40.2°, 46.9°, 49.7° and 53.3°, corresponding to various crystal planes. After being incorporated into the GN cryogel, the crystalline characteristics of nHAP still existed, as evidenced from the presence of the respective typical nHAP crystalline peaks. The crystalline peak associated with gelatin showed diminished intensity due to the high peak intensities of nHAP. It is noted that nHAP peaks in GN cryogel became slightly broader and weaker as compared with original nHAP, implying low crystallinity and smaller crystal size. Indeed, the average crystal grain size of embedded nHAP in GN cryogel was calculated to be 19.9 nm using the Scherrer equation and the diffraction peak at 2θ = 25.9°, which could be compared with that of HAP of 21.2 nm.

### 3.3 Swelling studies

When assessed as scaffolds for tissue engineering, the swelling behavior of cryogels is an important feature to evaluate since swelling increases the pore size and the surface area/volume ratio, thus facilitates the infiltration of cells into the 3D scaffolds.[45] Swelling of cryogels in water were measured through water uptake studies **(Fig. 2c)**. The water uptake values were similar initially but exhibited a marked difference after 1 min with higher values shown by G cryogels. The water uptake value reached ~90% for G cryogels at 10 min and remained constant thereafter. In contrast, GN cryogels reached the equilibrium value after 15 min at ~85%. Incorporation of nHAP in cryogel therefore only slightly decreased the equilibrium water absorption capability of the scaffold albeit replacing one-third of the organic polymer with ceramic particles. The swelling kinetics was further analyzed using equation (2). The fitted curves shown in **Fig. 2d** indicate that the model can satisfactorily predict water diffusion into cryogels. The respective values of $k$ and $n$ were found to be 0.662 and 0.138 for G cryogel ($r^2$ = 0.990) and 0.627 and 0.154 for GN cryogel ($r^2$ = 0.997). Faster swelling kinetics of G was confirmed from the higher $k$ value. Since the $n$ values for both cryogels are less than 0.5, the diffusion of water within the pores of both cryogels also occurred by a Fickian type mechanism during the swelling stage. This indicates water entered the inner region of the cryogel freely throughout the swelling process without the capillary effect due to long and wide aligned channels formed in the cryogels.

### 3.4 Thermogravimetric analysis (TGA)

To determine the thermal stability of cryogels, thermogravimetric analysis was performed to obtain the decomposition curves **(Fig. 3a)**. Similar to gelatin, the G cryogels showed an initial decomposition from 253 ºC and exhibited a peak thermal decomposition temperature at 319 ºC from the differential thermal decomposition curve **(Fig. 3b)**. A similar trend was observed for GN cryogels, in which the initial decomposition starts at the same temperature and the peak temperature remained the same. The percentage of weight retained in GN at 700 ºC was ~45% of the initial weight whereas in G it was ~20%, representing the effect of the non-thermal decomposable ceramic component (nHAP) in GN cryogels. The mass percentage of nHAP in GN cryogels could be calculated to be 31% from the residual weights, which is close to the value (33%) calculated from the initial weights of gelatin and nHAP used during preparation of GN cryogels. The thermal decomposition study revealed that GN cryogels maintained the same thermal stability as G cryogels at elevated temperatures, implying nHAP does not interrupt the

crosslinked structure of the organic part (gelatin) in the cryogel although at a lower degree of crosslinking.

### 3.5 Mechanical properties

The typical compressive stress-strain curves of the cryogels are shown in **Fig. 4a**. In accordance with the usual exponential stress-strain behavior shown by covalently cross-linked gels, the compressive stress-strain behavior of cryogels was non-linear and could be fitted satisfactorily with the empirical non-linear model shown in equation (3). The elastic moduli, calculated from the slopes of the stress-strain curves, changed continuously with stain during compression. The elastic moduli at 10%, 30% and 50% deformation were calculated from equation (3) and listed in **Table 1**. The elastic modulus increased slowly with strain up to 30% and showed no statistical difference between G and GN cryogels. It could be noted that the initial compressive moduli (10% strain) of G and GN cryogels are both within the range of 3D scaffolds preferred for osteogenic differentiation of mesenchymal stem cells reported by Huebsch et al., who demonstrated that osteogenic differentiation occurred predominantly at 11~30 kPa.[46] Nonetheless, the GN cryogel displayed a rapid increase in the elastic modulus at higher strain values, leading up to failure. Although not significantly different at 30% strain, the elastic modulus of GN was 1.5 times that of G at 50% strain. The failure strain of G was 52%, which is 30% less than that of GN. Most importantly, GN could withstand 14.4 times more stress than G at failure (**Table 1**). These stress-strain behaviors resulted in 11.5 times higher strain energy to failure (toughness) for GN than G cryogel. The quasi-static compression tests revealed that the mechanical properties of GN were significantly better than those of G. With comparable pore size and degree of crosslinking, this result could be attributed to the presence of nHAP in the cryogel strut, resulting in higher resistance to mechanical compression.

**Fig. 4b** shows the viscoelastic behavior of GH cryogels with the storage ($E'$) and viscous ($E''$) moduli measured using a frequency scan from 0.5 to 5 Hz. The values of both viscoelastic parameters are significantly higher for the composite GN cryogel, due to the presence of nHAP albeit of similar porosity to G cryogel. In particular, the value of the storage modulus ($E'$) at the frequency of 5 Hz for GN is 369 kPa, whereas the corresponding value for G is 288 kPa. The storage modulus represents the elastic component of a material and is an indicator of the

capability of a material to store energy during deformation.[47] **Fig. 4c** shows the variation of the loss tangent (tan δ) with the frequency. The loss tangent is the ratio between the amount of energy dissipated by viscous mechanisms and the energy stored in the elastic component, which provides information about the viscoelastic properties of the material.[48] The smaller the loss tangent is; the more elastic is the material. For both cryogels, the tan δ decreased with the increase of the frequency and reached 0.1 ($\delta \approx 6°$) with no significant difference between groups, indicating that nHAP did not influence the elasticity of the cryogel.

### 3.6 BMP-2 immobilized cryogel

Judging from the overall better physico–chemical and mechanical properties offered by GN, this cryogel was chosen to immobilize BMP-2 to enhance the regeneration potential by persuading osteo-induction environment for morphogenesis. The presences of induction factors are reported to accelerate the bone regeneration process and hence BMP-2 could be an ideal constituent for osteogenesis.[49,50] The SEM images of GNB cryogels shown in **Figs. 5a&b** confirm that BMP-2 binding had no significant influence on the macroporous structure of cryogels. The covalently bound BMP-2 in GNB cryogel is expected to maintain a sustained release profile for prolonged duration and thus could create an adequate environment for ADSCs to induce differentiation towards osteoblasts. The release profile of BMP-2 from GNB cryogels confirmed this release behavior under simulated conditions. The release was measured from the amount of BMP-2 in the release medium at specific time points to calculate the cumulative BMP-2 release percentage. Maximum amount of BMP-2 was released in the first 3 days, where the scaffold released ~30% of BMP-2, followed by a reduction in release rate in the following days till day 7 to attain the maximum accumulative release of 43% **(Fig. 5c)**. The sustained release profile up to 7 days confirms the covalent binding of BMP-2 in GNB cryogels. The sustained release of BMP-2 from GNB cryogels is expected to enhance the osteogenic differentiation of ADSCs by providing an osteo-inductive environment with copious BMP-2 around the cells during cell culture.

### 3.7 *In vitro* cell culture

#### 3.7.1 Cell proliferation assay and ALP activity

Rabbit ADSCs were used to evaluate the in vitro cell response of cryogel scaffolds. Cell attachment and proliferation were studied using the MTS assay **(Fig. 6a).** There is no statistical

difference in cell number at day 0 (4 h) among all groups, indicating nHAP and BMP-2 did not influence cell attachment. The cell numbers increased exponentially from day 1 to day 21 and reached saturation at day 28. Although the number of ADSCs increased with culturing time irrespective of the nature of the sample to endorse the biocompatibility of all cryogels, there is significant difference in cell proliferation rate with the trend G > GN > GNB. The G cryogel shows the highest cell proliferation rate (8.1-fold increase of cell number from day 0 to day 21) followed by GN (7.7-fold increase) and GNB (7.1-fold increase). It is reasonable to expect that ADSCs will lose their proliferation ability when induced into the osteogenic lineage. Since cell differentiation will lead to slower cell growth, the results indicate that osteogenic differentiation of ADSCs was enhanced in the presence of nHAP and maximized in the presence of a synergistic effect of nHAP and BMP-2.

The cell proliferation scenario in different cryogels could be further correlated with the ALP activity of ADSCs. Initiation of mineralization could be identified by recognizing the ALP marker. Nucleation starts with deposition of inorganic phosphates as $Ca^{2+}$ and thus results in calcification in local environment. Elevation in mineralization of cell extracellular matrix through the hydrolysis of phosphate esters causes a downstream cell differentiation factor to initiate differentiation and therefore, ALP can thus be considered as an effective measurement tool for the ADSCs differentiation to osteoblasts. The normalized values of ALP activities of ADSCs cultured in different cryogels are shown in **Fig. 6b**. The ALP activity significantly elevated at day 21 and declined at day 28 during cell culture in each group. While comparing among groups, G, GN and GNB cryogels had no significant difference in ALP activity at day 0, while GNB had higher level of ALP expression than G and N at day 7 with no difference between G and GN. However, the ALP activity at day 14 was significantly different among all cryogels, showing the effectiveness of both osteo-conductive and osteo-inductive factors in cell differentiation. The trend was followed on day 21, with maximum ALP expression for GNB followed by GN and G cryogels in descending order. The rationale behind the elevated ALP values of GN compared to G can be ascribed to the osteo-conductivity of nHAP component in the former. However, the combined effect of nHAP and BMP-2 in GNB accelerated ADSCs differentiation much faster than nHAP alone in GN and hence showed the highest ALP activity. The lowering of ALP activity at 28 days of culture could be correlated with the absence of ALP expression at later stages of cell differentiation. The trend of ALP expression at various time

points in different cryogels could depict the dominance of GNB scaffolds in ADSCs differentiation by the combined use of osteo-inductive and osteo-conductive factors, rather than using only the osteo-conductive factor (nHAP) in GN cryogel.

**3.7.2 Cell morphology and mineralization**

SEM/EDS analysis was performed to evaluate the morphology of cells in the cryogel scaffold after cultured for 14 days **(Fig. 6c-e).** ADSCs in G cryogel showed good cell spreading to connect the porous structure as visible from **Fig. 6c.** GN cryogel showed similar well-spread cell morphology within the scaffold **(Fig. 6d)**. However, GNB cryogels showed much better cell spreading compared to G and GN cryogels, presenting the dominance of BMP-2-incorporated scaffolds in introducing inducing effects on osteogenesis of ADSCs **(Fig. 6e)**. In addition, the presence of mineralized nodules on cell surface is higher for ADCSCs in GNB cryogel compared to G and GN cryogels and thus denotes the effective mineralization of ADSCs in the presence of the combined environment of conductive-inductive factors. Mineralization is the process of calcium phosphate deposition on the substrate surface.[51,52]. The prime evidence of stem cell differentiation is the mineralization of inorganic phosphates on substrate surface at the middle of the differentiation period. This could be identified both qualitatively and quantitatively, in which white mineral deposition in SEM image could be considered as the qualitative proof while elemental analysis by EDS would be an easy tool for the qualitative estimation. The EDS analysis was thus used to measure the atomic percentages of elements present in the deposited minerals on the cell surface during ADSCs differentiation.[53] Since the major component of cortical bone is calcium phosphate in the form of hydroxyapatite with an ideal Ca to P ratio of 1.67, similar ratio of mineral deposition is much preferable for ideal bone regeneration process. Insets of **Figs. 6c-e** are the EDS spectra of minerals deposited on ADSCs, cultured in cryogels for 14 days. The measured Ca/P ratio of G, GN and GNB cryogels were 1.99, 1.56 and 1.45, respectively, which are relatively close to the theoretical value 1.67. The atomic percentage values of Ca and P thus confirms the suitability of cryogels as bone tissue engineering scaffolds.

**3.7.3 Live-dead assay and cytoskeletal arrangement**

Cellular viability of ADSCs in cryogel scaffolds were analyzed through the live-dead staining assay. Though MTS assay confirmed the increase of number of viable cells in various cryogel scaffolds, the same was re-confirmed through fluorescent staining of cells and observed with confocal microscopy. **Fig. 7a** shows the morphology of cells in G, GN and GNB cryogels

respectively at day 14, with green color representing live cells and red color denoting possible dead cells. Relatively negligible amount of red stains appeared in the images, underlining the biocompatibility of all cryogels. Although the substrate-specific differentiation of ADSCs couldn't be concluded from the confocal images, as no significant difference in cell morphology could be found; however, a well-defined cuboidal morphology is visible in all cryogels at day 14, indicating the early differentiation of cells toward the osteogenic lineage. Thus the live-dead assay further confirms the biocompatibility of cryogel scaffolds towards ADSCs. The confocal images were further gathered when cells were stained with DAPI and phalloidin for nuclear and F-actin staining, respectively **(Fig. 7b)**. Phalloidin conjugation displayed well organized arrangements of cytoskeleton while DAPI staining confirms the presence of nucleus. Similar to live-dead staining, nuclear-cytoskeleton imaging further endorses the cyto-compatibility of cryogels. Filopodial extensions were much visible in confirming the well-organized arrangements of well-spread ADSCs in all cryogels.

**3.7.4 Quantification of Osteocalcin**

The protein concentration analysis was performed to estimate the quantity of OCN produced during ADSCs culture at day 7, 14 and 28 **(Fig. 7c)**. Compared to day 7, the OCN protein level was significantly higher at day 14 and 28. There was no significant difference in OCN production at day 14 and 28, implies the saturation of protein production at later stages. As OCN is produced at the later stage of osteogenic differentiation, the higher concentrations at 14 and 28 days are justifiable. Moreover, the trend in OCN production shows the maximum value for GNB cryogel and the minimum for G cryogel at 14 and 28 days, implying the combined effects of both osteo-conductive and osteo-inductive factors on ADSCs differentiation to a bone-specific lineage. This could be correlated with the highest ALP activity shown by ADSCs in GNB cryogel in **Fig 6b**.

**3.7.5 Gene expression**

In osteogenic differentiation, cells mainly express three transformations called proliferation, maturation and mineralization. During differentiation, ADSCs will bring up up-down regulations of certain genes, with expression of various marker proteins at early, mid and later stages of cell differentiation. The major osteogenic differentiation marker genes includes COL I, ALP, OCN, OPN etc. and their presence could be verified from the relative mRNA expressions of ADSCs cultured in different scaffolds for different durations. Among various markers, COL I and ALP

belong to the early differentiation stage whereas OCN and OPN are expressed at mid-later stages of ADSCs osteogenic differentiation. The relative mRNA expression of COL I and OPN are shown in **Fig. 8.** Being an early marker of cell differentiation, COL I was up-regulated on day 7 and further time points displayed a down-regulated expression on day 14, 21 and 28. This trend of COL I down regulation at later stages of cell culture confirms the proper osteogenic differentiation of ADSCs. Apart from the duration of culture, the effect of osteo-conductive and/or osteo-inductive factors in controlling the up-down regulations of COL I in different cryogel samples was verified. GNB cryogel showed pronounced increase of COL I gene expression over G and GN cryogels from day 7 to 28. There was also significant difference in COL I expression between G and GN cryogels from day 14 to 28. Osteogenic differentiation was further evaluated on the basis of the late marker OPN. In contrast to COL I, the expression was lower on day 7 and increased successively to reach a maximum on day 21. It also showed significant different expression levels among groups up to this time point. The higher expression levels of OPN at the later stages of cell culture cross-confirms the osteogenic differentiation of ADSCs. Similar to COL I, GNB depicted the maximum OPN expression compared to other cryogels.

### 3.8 In vivo animal studies

#### 3.8.1 Computed tomography

Based on the in vitro results, acellular and cell-seeded GNB cryogels were studied for bone regeneration in the critical cranial bone defect model in rabbits with allogenic ADSCs. **Fig. 9a** shows the acellular cryogel and the ADSCs/cryogel construct (cultured for 21 days in vitro) prior to implantation. **Fig. 9b** shows the created cranial defects to be filled with the acellular cryogel (right) and the ADSCs/cryogel construct (left). Sixteen weeks after implantation, all the animals were anesthetized, sacrificed and evaluated for bone formation by histology and IHC. At necropsy, all the recipient sites implanted with tested materials displayed normal-appearing tissues with neither swelling nor tissue necrosis. In addition, there were no clinical complications (e.g., infection, wound breakdown, or exudate) detected at the implant sites.

The animals underwent CT for evaluating the bone formation at 1 and 16 weeks post-operation (**Fig. 9c**). The CT images showed similar image density in the acellular and ADSCs/cryogel groups 1 week post-operation. The image density of the acellular group did not

increase very prominently at 16 weeks compared to 1 week post-operation. Conversely, the image density of the ADSCs/cryogel group elevated obviously at 16 weeks compared to 1 week post-operation. For quantification of the mineralization and density at the implant area, the Hounsfield units (HU) with 8 repeated data were calculated for both groups and normal bone by the OsiriX software (**Figure 9d)**. Schreiber et al. described that the HU was correlated with dual X-ray absorptiometry bone mineral density measurements and mechanical strength so that it could be used as an alternative tool for determining the regional bone mineral density.[54]At week 1 post-operation, the HU were not significantly different between groups but it showed significant difference at week 16. The HU increased significantly with time only for the ADSCs/cryogel group with the HU increase 12.5-fold from week 1 to week 16. In contrast, the time-dependent elevation was not significant for the acellular group. These results indicated that new bone formation was only possible with transplanted allogenic ADSCs in GNB cryogel. Comparing to the HU of normal bone surrounding the defect, we found the HU of ADSCs/cryogel at 16 weeks were around 59% that of normal bone (HU = 1418 ± 119). This means that the implanted ADSCs/cryogel construct could achieve 59% of the mechanical strength of normal bone within 16 weeks of implantation. Alternatively, osteogenesis could be verified from the new bone volumes at week 16, which were 9.2 and 66.6 $mm^3$ for acellular cryogel and ADSCs/cryogel groups, respectively.

**3.8.2 Histological evaluation and IHC staining**

Bone formation and tissue development was further confirmed through histological evaluation, including H&E and Masson's trichrome staining, and IHC staining of COL I and OCN (**Fig. 10**). The H&E staining validates the number of osteoblasts in the defect region is much higher for the ADSCs/cryogel group compared with the acellular control group, indicating bone growth in the defect region. The existence of osteoid (purple color) with osteoblasts in the bone matrix further confirms that the ADSCs/cryogel group shows mature bone in the defect region with the formation of new osteoid bodies. However, the acellular control scaffold displayed neither osteoid nor osteoblasts in the interior, and also the empty scaffold cross-section morphology confirming no tissue regeneration.

ADSCs differentiation was further verified through Masson's trichrome staining. The deep blue-colored stains in the sections of ADSCs-seeded scaffold confirm the osteoid formation. When ADSCs differentiated into osteoblasts, osteoid will be embedded in the newly

formed tissue matrix and thus could be proved through staining. In contrast, acellular control scaffold had significantly low level of staining in which empty cross-sections of scaffold is more visible. Bone regeneration was further evaluated through IHC staining of COL I and OCN, in which the former is an early marker while the latter is a mid-later stage marker of osteogenic differentiation. Considering the ADSCs-seeded scaffold, both COL I and OCN displayed intense brown stains compared to the acellular scaffold. That the staining intensity of intense brown color was much higher for OCN and COL I in the ADSCs/cryogel group confirms continued proliferation and osteogenic differentiation of ADSCs in vivo. Similar to H&E or Masson's trichrome staining, the acellular cryogel scaffold did not display positive IHC staining. The purple color in the ADSCs-seeded scaffold could be attributed to the existence of cell nuclei, which is absent in the control group. Taken together, both histology and IHC staining results confirm the ideal candidacy of GNB cryogels in bone tissue engineering, conjoining the combinational effect of osteo-conductive nHAP and osteo-inductive BMP-2 in a single system.

## 4. Conclusion

Macroporous cryogels for bone tissue engineering could be fabricated from gelatin alone (G) or gelatin/nHAP (GN) to obtain cryogel scaffolds with different properties. SEM confirmed reproducible porous morphology for all the cryogel scaffolds, with slightly broader pore size distribution for G than GN scaffolds. GN cryogel showed improved mechanical properties compared to G cryogel from compression testing, while swelling kinetics confirmed the faster water uptake nature of G cryogels. The osteo-conductive GN cryogel was further modified by covalently binding with BMP-2 to obtain GNB cryogels endowed with a sustained release behavior of BMP-2. When seeded with rabbit ADSCs, the cell proliferation studies endorsed the biocompatibility of the scaffold while ALP activity and OCN protein production rationalized the highest osteogenic differentiation potential of ADSCs in GNB cryogels. The relative mRNA expression of osteogenic marker genes also underlined the highest osteogenesis potential of ADSCs in GNB cryogels in vitro. Based on the histological and IHC staining of the phenotypic markers for osteogenesis, successful bone formation was confirmed when allogenic ADSCs were seeded in GNB cryogels to repair critical size calvarial defects in rabbits. The bone formation could be further confirmed through CT analysis to prove the combined applicability of osteo-conductive and osteo-inductive factors in GNB cryogel towards enhanced bone regeneration.

**Acknowledgements**

This work was supported by Chang Gung Memorial Hospital (BMRP249, CMRPD3D0201-2 and CMRPG3E0561) and Ministry of Science and Technology (MOST), Taiwan, ROC (NMRPG3E0471). The Microscope Core Laboratory, Chang Gung Memorial Hospital, Linkou is acknowledged for the expert technical assistance.

**References**

1. D. L. Butler, S. A. Goldstein and F. Guilak, *Journal of Biomechanical Engineering*, 2000, **122**, 570-575.
2. S. MacNeil, *Materials Today*, 2008, **11**, 26-35.
3. D. K. Bishi, S. Mathapati, J. R. Venugopal, S. Guhathakurta, K. M. Cherian, S. Ramakrishna and R. S. Verma, *Journal of Materials Chemistry B*, 2013, **1**, 3972-3984.
4. S. K. L. Levengood and M. Zhang, *Journal of Materials Chemistry B*, 2014, **2**, 3161-3184.
5. J.-P. Chen and C.-H. Su, *Acta biomaterialia*, 2011, **7**, 234-243.
6. A. R. Amini, C. T. Laurencin and S. P. Nukavarapu, *Critical Reviews in Biomedical Engineering*, 2012, **40**, 363-408.
7. D. W. Hutmacher, *Biomaterials*, 2000, **21**, 2529-2543.
8. K. J. L. Burg, S. Porter and J. F. Kellam, *Biomaterials*, 2000, **21**, 2347-2359.
9. K. Rezwan, Q. Z. Chen, J. J. Blaker and A. R. Boccaccini, *Biomaterials*, 2006, **27**, 3413-3431.
10. K. T. Shalumon, K. H. Anulekha, K. P. Chennazhi, H. Tamura, S. V. Nair and R. Jayakumar, *International Journal of Biological Macromolecules*, 2011, **48**, 571-576.
11. P. X. Ma, R. Zhang, G. Xiao and R. Franceschi, *Journal of Biomedical Materials Research*, 2001, **54**, 284-293.
12. M. M. Stevens, *Materials Today*, 2008, **11**, 18-25.
13. M. N. Khan, J. M. Islam and M. A. Khan, *Journal of Biomedical Materials Research. Part A*, 2012, **100**, 3020-3028.
14. X. Liu, L. A. Smith, J. Hu and P. X. Ma, *Biomaterials*, 2009, **30**, 2252-2258.
15. C. He, F. Zhang, L. Cao, W. Feng, K. Qiu, Y. Zhang, H. Wang, X. Mo and J. Wang, *Journal of Materials Chemistry*, 2012, **22**, 2111-2119.
16. Y. Kimura, M. Ozeki, T. Inamoto and Y. Tabata, *Biomaterials*, 2003, **24**, 2513-2521.
17. C. M. Murphy, M. G. Haugh and F. J. O'Brien, *Biomaterials*, 2010, **31**, 461-466.
18. S. H. Li, J. R. De Wijn, P. Layrolle and K. De Groot, *Journal of Biomedical Materials Research*, 2002, **61**, 109-120.
19. Q. Hou, D. W. Grijpma and J. Feijen, *Biomaterials*, 2003, **24**, 1937-1947.
20. Y. S. Nam and T. G. Park, *Biomaterials*, 1999, **20**, 1783-1790.
21. S. M. Tommasini, P. Nasser, M. B. Schaffler and K. J. Jepsen, *Journal of Bone and Mineral Research*, 2005, **20**, 1372-1380.
22. A. Abdal-hay, T. Amna and J. K. Lim, *Solid State Sciences*, 2013, **18**, 131-140.

23. S.-I. Roohani-Esfahani, S. Nouri-Khorasani, Z. Lu, R. Appleyard and H. Zreiqat, *Biomaterials*, 2010, **31**, 5498-5509.
24. P. S. Eggli, W. Muller and R. K. Schenk, *Clinical Orthopaedics & Related Research*, 1988, 127-138.
25. W. Zhang, C. Zhu, Y. Wu, D. Ye, S. Wang, D. Zou, X. Zhang, D. L. Kaplan and X. Jiang, *European Cells & Materials*, 2014, **27**, 1-11; discussion 11-12.
26. G. Chen, C. Deng and Y.-P. Li, *International Journal of Biological Sciences*, 2012, **8**, 272-288.
27. C. Niedhart, U. Maus, O. Miltner, H. G. Graber, F. U. Niethard and C. H. Siebert, *Journal of Biomedical Materials Research. Part A*, 2004, **69**, 680-685.
28. S. E. Lynch, D. Buser, R. A. Hernandez, H. P. Weber, H. Stich, C. H. Fox and R. C. Williams, *Journal of Periodontology*, 1991, **62**, 710-716.
29. S. R. Thaller, M. A. Salzhauer, A. J. Rubinstein, A. Thion and H. Tesluk, *Journal of Craniofacial Surgery*, 1998, **9**, 138-141.
30. K. H. Chang, H. T. Liao and J. P. Chen, *Acta Biomaterialia*, 2013, **9**, 9012-9026.
31. C. Y. Kuo, C. H. Chen, C. Y. Hsiao and J. P. Chen, *Carbohydrate Polymers*, 2015, **117**, 722-730.
32. G. J. Lai, K. T. Shalumon and J. P. Chen, *International Journal of Nanomedicine*, 2015, **10**, 567-584.
33. J. S. Pieper, T. Hafmans, J. H. Veerkamp and T. H. van Kuppevelt, *Biomaterials*, 2000, **21**, 581-593.
34. A. F. Habeeb, *Analytical Biochemistry*, 1966, **14**, 328-336.
35. W. Xue, S. Champ, M. B. Huglin and T. G. J. Jones, *European Polymer Journal*, 2004, **40**, 467-476.
36. A. R. Khare and N. A. Peppas, *Biomaterials*, 1995, **16**, 559-567.
37. S. L. Woo, M. A. Gomez and W. H. Akeson, *Journal of Biomechanical Engineering*, 1981, **103**, 293-298.
38. E. Arrigoni, S. Lopa, L. de Girolamo, D. Stanco and A. T. Brini, *Cell and Tissue Research*, 2009, **338**, 401-411.
39. G. J. Lai, K. T. Shalumon, S. H. Chen and J. P. Chen, *Carbohydrate Polymers*, 2014, **111**, 288-297.
40. S. Bose, S. Vahabzadeh and A. Bandyopadhyay, *Materials Today*, 2013, **16**, 496-504.
41. V. Karageorgiou and D. Kaplan, *Biomaterials*, 2005, **26**, 5474-5491.
42. M. C. Chang, C. C. Ko and W. H. Douglas. *Biomaterials*, 2003, **24**, 2853-2862.
43. M. C. Chang and H. K. Yang. *Journal of the Korean Ceramic Society*, 2012, **49**, 72-77.
44. C. S. Ki, D. H. Baek, K. D. Gang, K. H. Lee, I. C. Um and Y. H. Park, *Polymer*, 2005, **46**, 5094-5102.
45. R. Jayakumar, R. Ramachandran, P. T. Sudheesh Kumar, V. V. Divyarani, S. Srinivasan, K. P. Chennazhi, H. Tamura and S. V. Nair, *International Journal of Biological Macromolecules*, 2011, **49**, 274-280.
46. N. Huebsch, P. R. Arany, A. S. Mao, D. Shvartsman, O. A. Ali, S. A. Bencherif, J. Rivera-Feliciano and D. J. Mooney, *Nature Materials*, 2010, **9**, 518-526.
47. F. G. Torres, S. N. Nazhat, S. H. Sheikh Md Fadzullah, V. Maquet and A. R. Boccaccini, *Composites Science and Technology*, 2007, **67**, 1139-1147.
48. W. Santawisuk, W. Kanchanavasita, C. Sirisinha and C. Harnirattisai, *Dental Materials Journal*, 2010, **29**, 454-460.

49. J. Park, J. Ries, K. Gelse, F. Kloss, K. von der Mark, J. Wiltfang, F. W. Neukam and H. Schneider, *Gene Therapy*, 2003, **10**, 1089-1098.
50. K. T. Shalumon, G.-J. Lai, C.-H. Chen and J.-P. Chen, *ACS Applied Materials & Interfaces*, 2015, **7**, 21170-21181.
51. S. Heinemann, C. Heinemann, R. Bernhardt, A. Reinstorf, B. Nies, M. Meyer, H. Worch and T. Hanke, *Acta Biomaterialia*, 2009, **5**, 1979-1990.
52. G. Toskas, C. Cherif, R.-D. Hund, E. Laourine, B. Mahltig, A. Fahmi, C. Heinemann and T. Hanke, *Carbohydrate Polymers*, 2013, **94**, 713-722.
53. J. P. Chen and Y. S. Chang, *Colloids and Surfaces. B, Biointerfaces*, 2011, **86**, 169-175.
54. J. J. Schreiber, P. A. Anderson, H. G. Rosas, A. L. Buchholz and A. G. Au, *Journal of Bone and Joint Surgery. American Volume*, 2011, **93**, 1057-1063.

Table 1. Mechanical properties of G and GN cryogel. Values are the mean ± SD of five independent measurements.

| | G | GN |
|---|---|---|
| Compressive elastic modulus at ε = 10% (kPa) | 14.6 ± 4.7 | 11.6 ± 1.8 |
| Compressive elastic modulus at ε = 30% (kPa) | 55.6 ± 0.4 | 57.0 ± 16.1 |
| Compressive elastic modulus at ε = 50% (kPa) | 201.7 ± 20.9 | 295.7 ± 50.1 |
| Compressive strain to failure, $\varepsilon_{max}$ (%) | 52.0 ± 1.0 | 82.2 ± 1.4 |
| Compressive stress to failure, $\sigma_{max}$ (kPa) | 34.6 ± 1.6 | 498.4 ± 27.1 |
| Toughness ($kJ/m^3$) | 5.4 ± 0.6 | 62.0 ± 2.9 |

## Figure Legends

**Fig. 1.** (a) Scanning electron microscopy (SEM)/energy dispersive spectroscopy (EDS) analysis and (b) the pore size distribution of G and GN cryogels. The EDS spectra are shown in the inserts of (a). The pore size distribution in (b) was determined by capillary flow porometry.

**Fig. 2.** (a) Fourier transform infrared (FTIR) analysis, (b) X-ray diffraction (XRD) analysis and (c, d) the swelling kinetics of G and GN cryogels. The water uptake in (c) was calculated from $W_t/M_{eq}\times100$, where $W_t$ and $M_{eq}$ are the mass of water absorbed at time t and the mass of cryogel at equilibrium, respectively. The lines shown in (d) are curves fitted with $W_t/W_{eq} \times 100 = kt^n$, where $W_t$ and $W_{eq}$ are the mass of water absorbed at time $t$ and at equilibrium, respectively.

**Fig. 3.** Thermogravimetric analysis of G and GN cryogel in terms of weight loss (a) and derivative weight (b).

**Fig. 4.** (a) Compressive mechanical properties and (b, c) viscoelastic properties of G and GN cryogels. (a) Stress–strain curves; (b) storage modulus ($E'$) and loss modulus ($E''$); (c) loss tangent (tan δ).

**Fig. 5.** (a, b) SEM micrographs of BMP-2 loaded (GNB) cryogels. (c) The release profiles of BMP-2 from GNB cryogels.

**Fig. 6.** (a) Proliferation, (b) normalized alkaline phosphatase (ALP) activity, and (c-e) SEM/EDS analysis of rabbit adipose-derived stem cells (ADSCs) in G, GN and GNB cryogels. The EDS spectra are shown in the inserts of c to e. Scale bar = 20 μm. *$p < 0.05$ compared with G cryogels, $^{\#}p<0.05$ compared with GN cryogels.

**Fig. 7.** (a) Live/dead staining (scale bar = 100 μm), (b) phalloidin-DAPI staining (scale bar = 50 μm) by confocal laser scanning microscopy after 14 days and (c) quantitative evaluation of osteocalcin (OCN) production of rabbit adipose-derived stem cells (ADSCs) in G, GN and GNB cryogels. *$p < 0.05$ compared with G cryogel, $^{\#}p<0.05$ compared with GN cryogel.

**Fig. 8.** (a) Type I collagen (Col I) and (b) osteopontin (OPN) mRNA expression of rabbit adipose-derived stem cells (ADSCs) in G, GN and GNB cryogels at various time points. The relative Q-PCR values were corrected using the glyceraldehyde-3-phosphate dehydrogenase (GAPDH) expression levels and normalized with respect to the values on day 0 of culture. *$p < 0.05$ compared with G cryogel, $^{\#}p<0.05$ compared with GN cryogel.

**Fig. 9.** (a) Photographs of GNB cryogels seeded with rabbit adipose-derived stem cells (ADSCs/cryogel) and control (acellular cryogel) GNB cryogels prior to implantation. (b) The rabbit calvarial defects were filled with implanted cryogels. The left defect was filled with ADSCs/cryogel constructs while the right defect was filled with acellular cryogels. (c) The computed tomography (CT) scanning images and (d) the Hounsfield units (HU) of bone regeneration in the rabbit calvarial critical size defects 1 and 16 weeks post-operation. The arrows refer to the defects filled with ADSCs/GNB cryogel constructs while the arrowheads indicate the defects filled with acellular GNB cryogels. The OsiriX image software was used to calculate the average HU values by outlining the bone defect region in the 2D cross-sectional views.

**Fig. 10.** Histological (H&E, Masson's trichrome) and immunohistochemical (COL I and OCN) examinations of implanted cryogels in rabbit calvarial defects 1 and 16 weeks post-operation. GNB cryogels seeded with rabbit adipose-derived stem cells (ADSCs/cryogel) was the test sample while GNB cryogels (acellular cryogel) was the control. Scale bar = 200 μm.

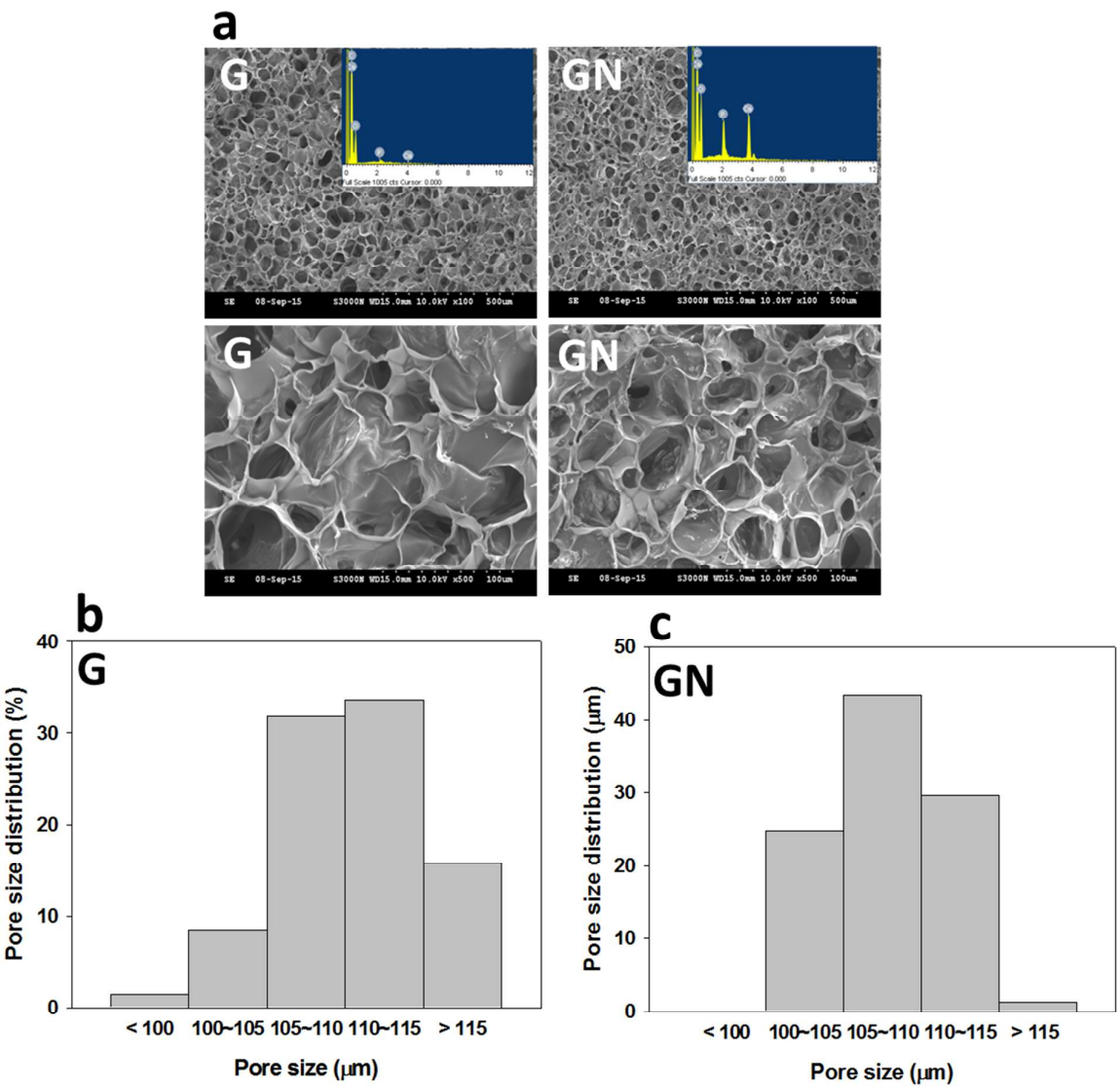
a
G
GN
G
GN
b
G
Pore size distribution (%)
40
30
20
10
0
< 100
100~105
105~110
110~115
> 115
Pore size (μm)
c
GN
Pore size distribution (μm)
50
40
30
20
10
0
< 100
100~105
105~110
110~115
> 115
Pore size (μm)

**Fig. 1**

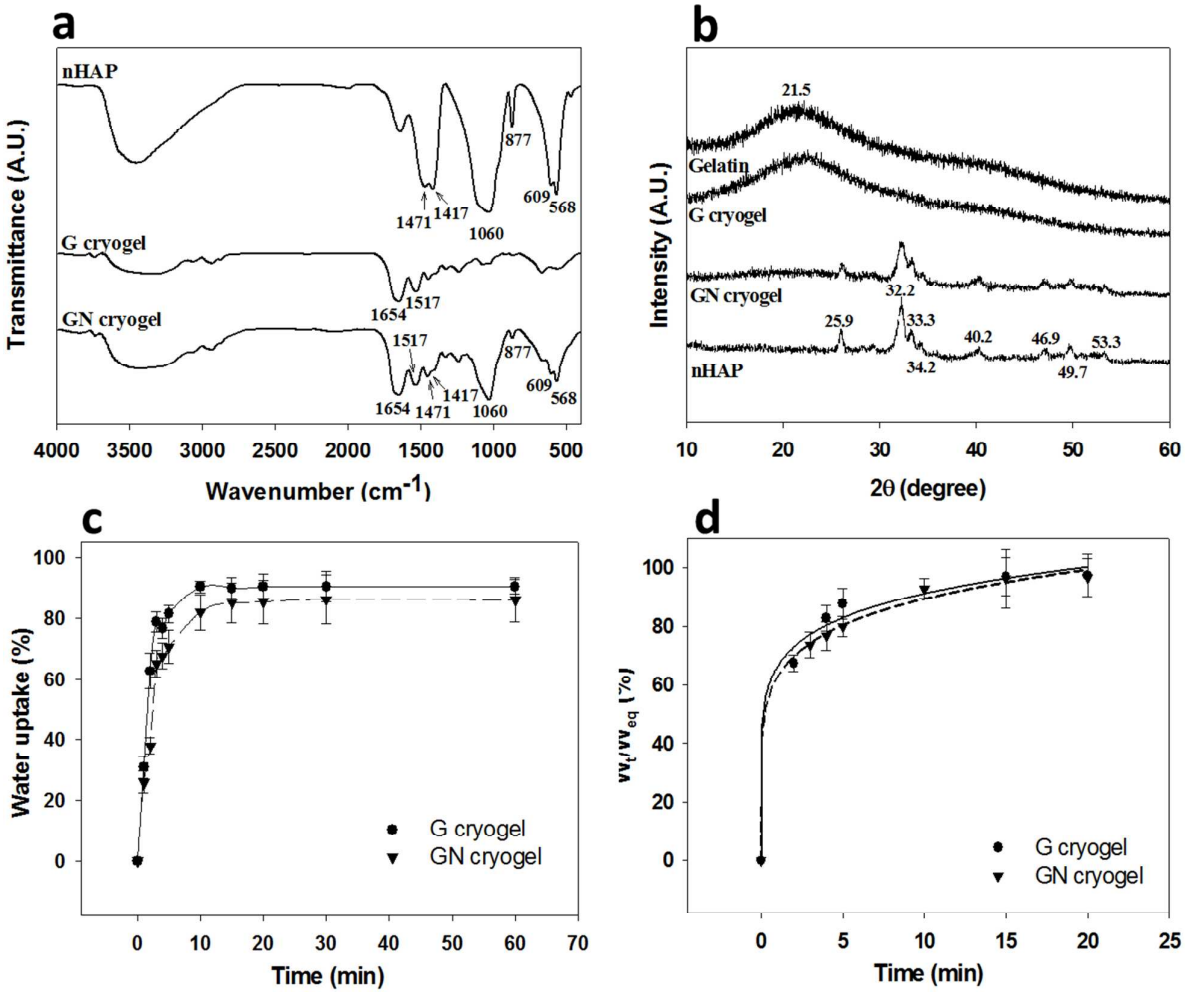
a
nHAP
G cryogel
GN cryogel
Transmittance (A.U.)
Wavenumber (cm-1)
1471
1417
1060
877
609
568
1654
1517
b
Gelatin
G cryogel
GN cryogel
nHAP
Intensity (A.U.)
2θ (degree)
21.5
32.2
25.9
33.3
40.2
46.9
53.3
34.2
49.7
c
Water uptake (%)
Time (min)
G cryogel
GN cryogel
d
Time (min)
G cryogel
GN cryogel

**Fig. 2**

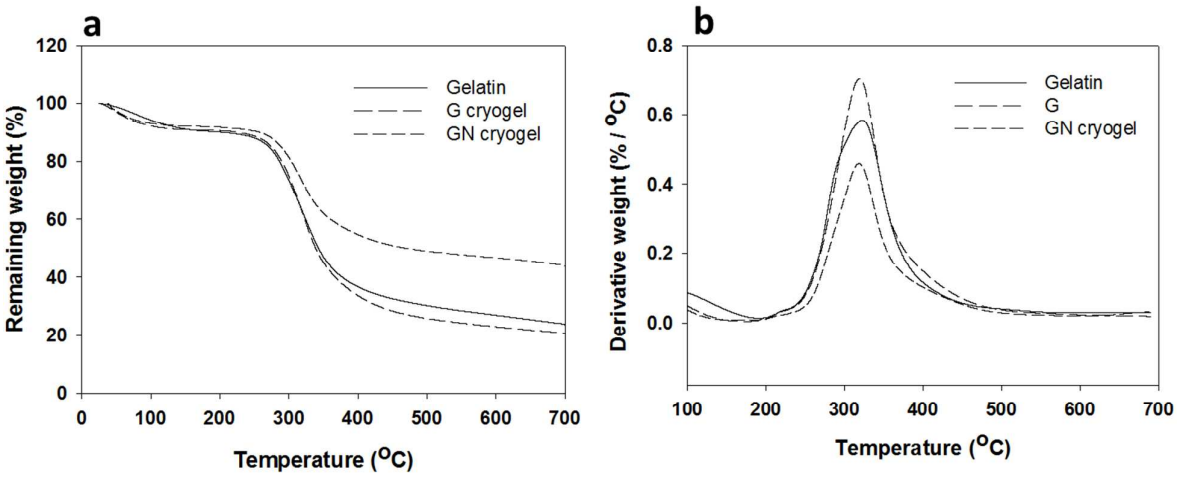
a
Remaining weight (%)
Temperature (°C)
Gelatin
G cryogel
GN cryogel
b
Derivative weight (% / °C)
Temperature (°C)
Gelatin
G
GN cryogel

**Fig. 3**

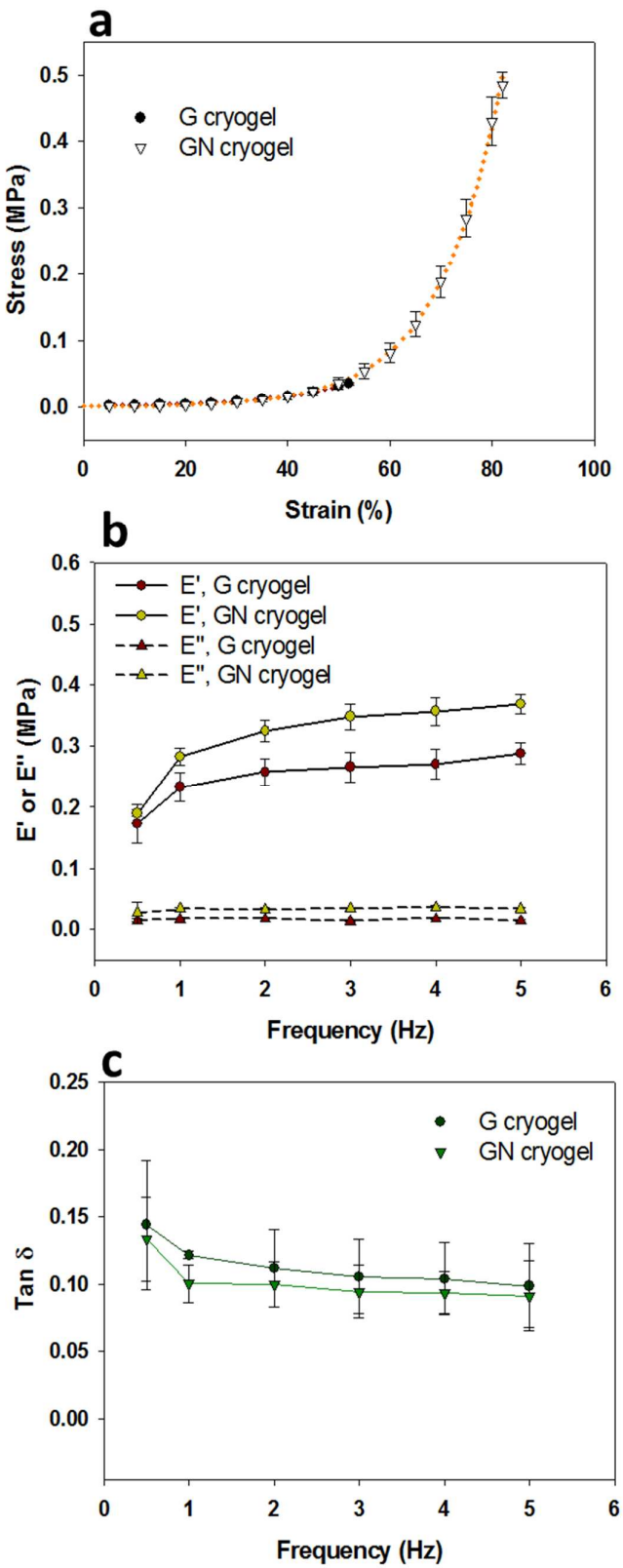
a
G cryogel
GN cryogel
Stress (MPa)
Strain (%)
b
E', G cryogel
E', GN cryogel
E'', G cryogel
E'', GN cryogel
E' or E'' (MPa)
Frequency (Hz)
c
G cryogel
GN cryogel
Tan δ
Frequency (Hz)

**Fig. 4**

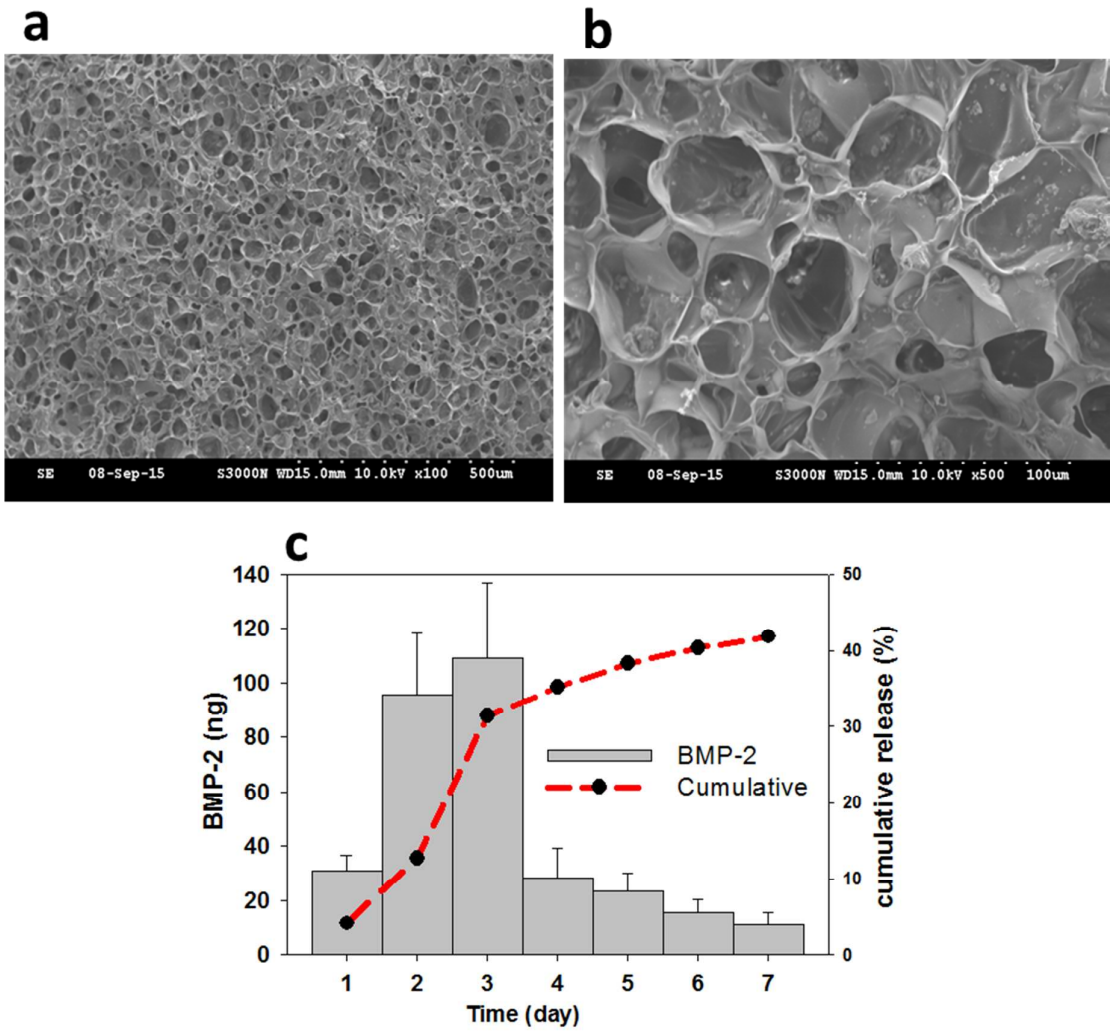
a
b
SE 08-Sep-15 S3000N WD15.0mm 10.0kV x100 500um
SE 08-Sep-15 S3000N WD15.0mm 10.0kV x500 100um
c
BMP-2 (ng)
cumulative release (%)
Time (day)
BMP-2
Cumulative
0
20
40
60
80
100
120
140
0
10
20
30
40
50
1
2
3
4
5
6
7

**Fig. 5**

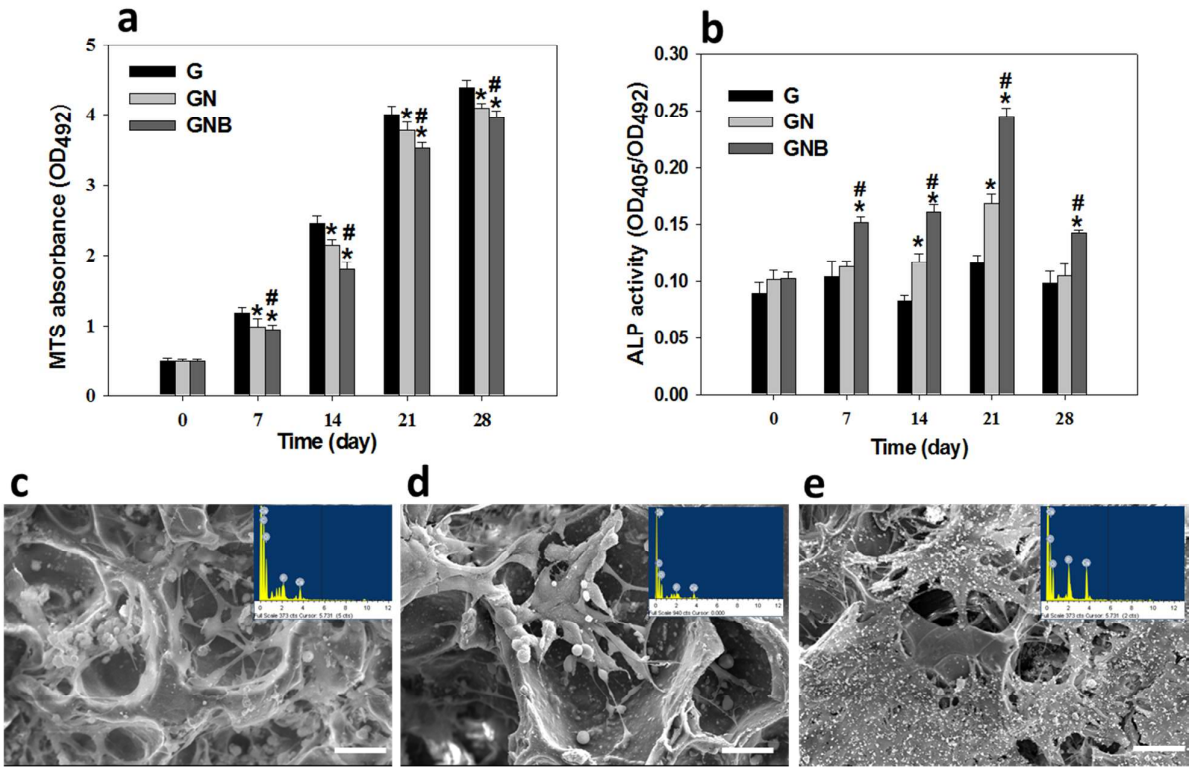
a
MTS absorbance (OD492)
G
GN
GNB
Time (day)
b
ALP activity (OD405/OD492)
G
GN
GNB
Time (day)
c
d
e

**Fig. 6**

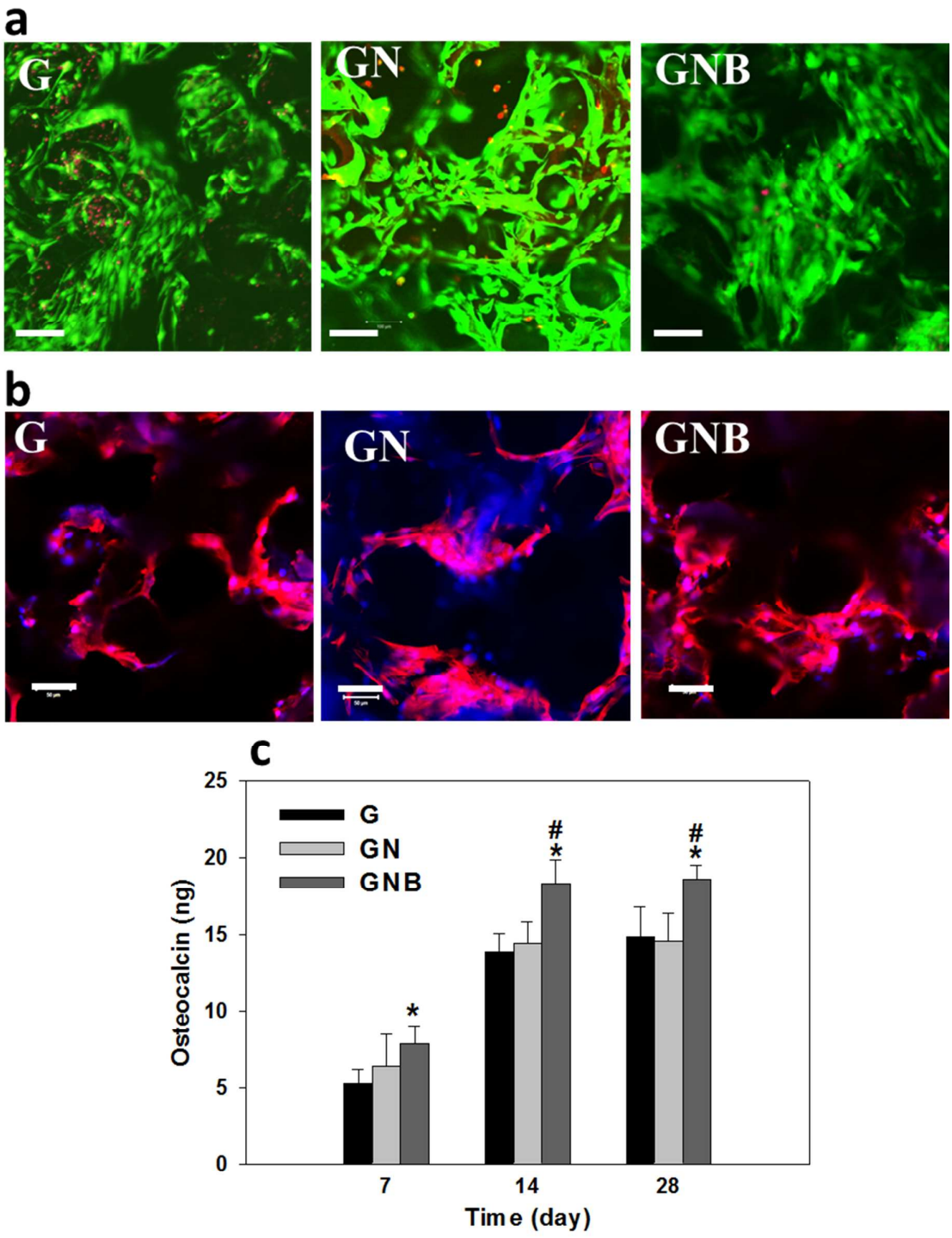
a
G
GN
GNB
b
G
GN
GNB
c
Osteocalcin (ng)
25
20
15
10
5
0
G
GN
GNB
*
#
*
#
*
7
14
28
Time (day)

Fig. 7

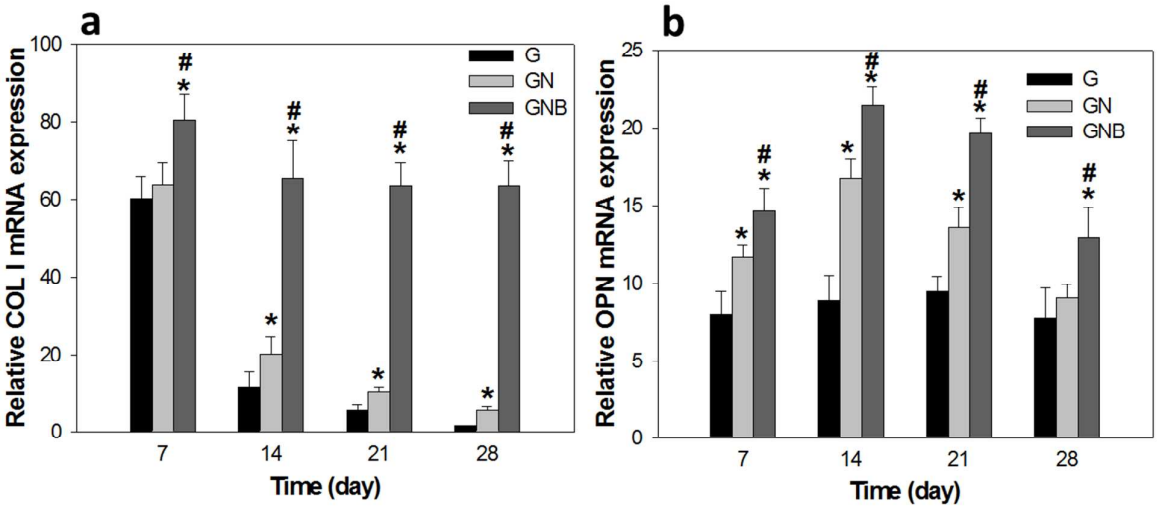
a
Relative COL I mRNA expression
100
80
60
40
20
0
7
14
21
28
Time (day)
G
GN
GNB
b
Relative OPN mRNA expression
25
20
15
10
5
0
7
14
21
28
Time (day)
G
GN
GNB

**Fig. 8**

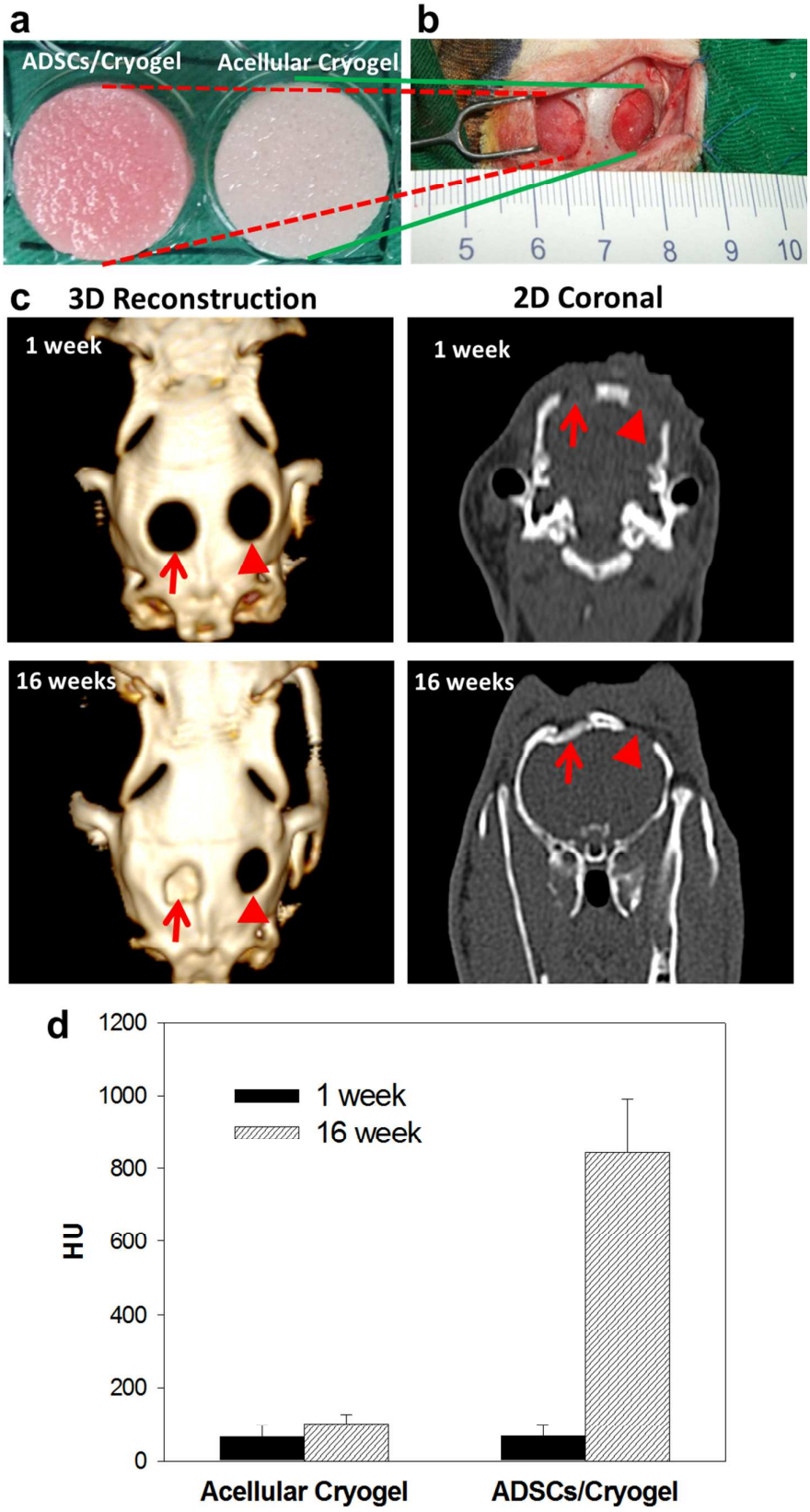
a
ADSCs/Cryogel
Acellular Cryogel
b
5
6
7
8
9
10
c
3D Reconstruction
2D Coronal
1 week
1 week
16 weeks
16 weeks
d
HU
1200
1000
800
600
400
200
0
1 week
16 week
Acellular Cryogel
ADSCs/Cryogel

Fig. 9

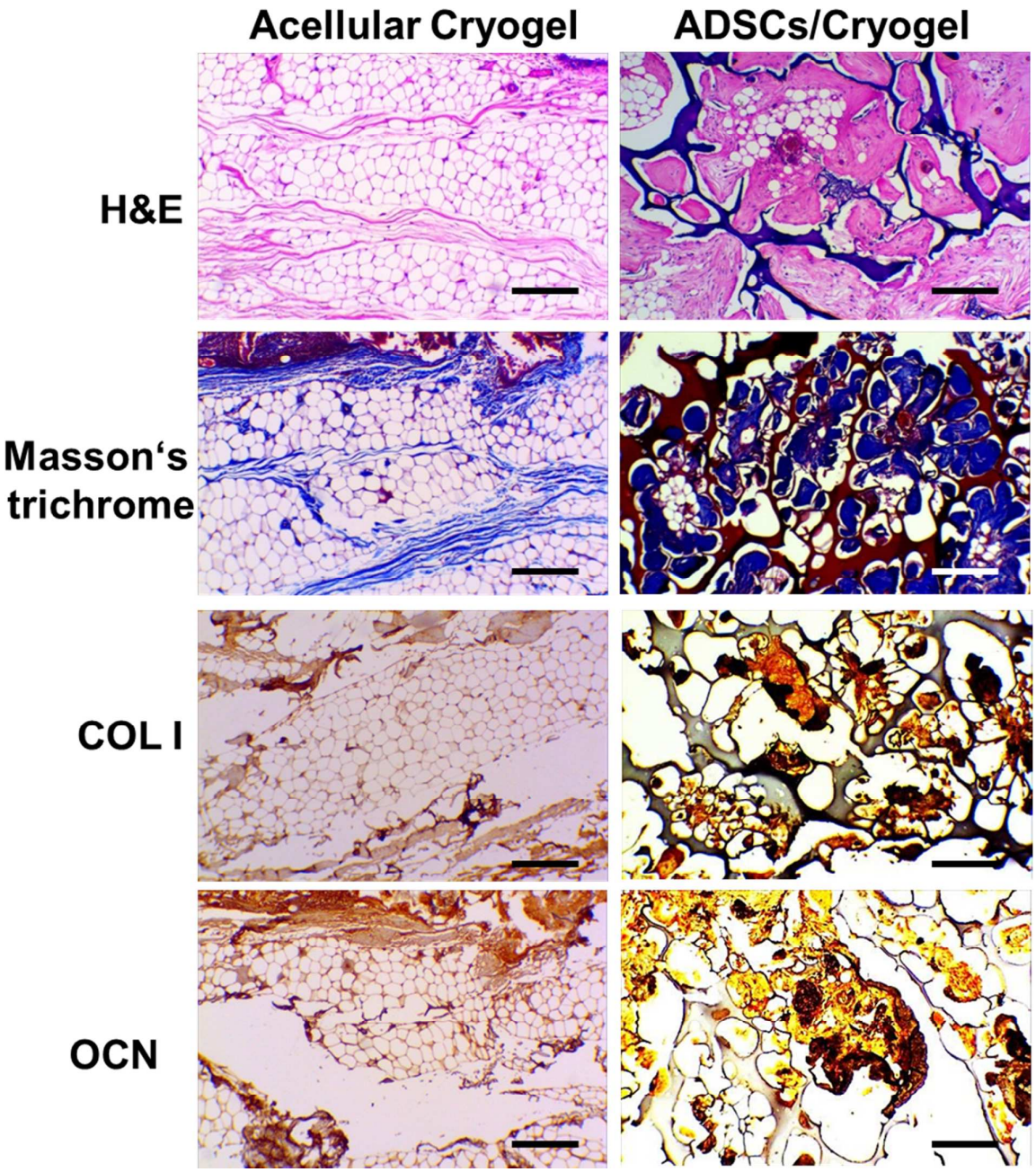
Acellular Cryogel
ADSCs/Cryogel
H&E
Masson's trichrome
COL I
OCN

Fig. 10

# Table of Contents

Gelatin cryogels modified with nHAP and BMP-2 could provide cues to promote osteogenesis of ADSCs in vitro and in vivo.